Numerical modelling of sound radiation and transmission in buildings using the time-domain nodal discontinuous Galerkin method

Sihar, Indra; Yang, Jieun; Hornikx, Maarten

DOI
10.1016/j.apacoust.2024.110197

Publication date
2024

Document Version
Final published version

Published in
Applied Acoustics

Applied Acoustics 225 (2024) 110197

Contents lists available at ScienceDirect

Applied Acoustics

journal homepage: www.elsevier.com/locate/apacoust

Numerical modelling of sound radiation and transmission in buildings using the time-domain nodal discontinuous Galerkin method

Indra Sihar [a,b,*], Jieun Yang [c], Maarten Hornikx [d]

[a] School of Electrical Engineering and Informatics, Bandung Institute of Technology, Ganesa 10, 40132, Bandung, Indonesia
[b] Research Center for Information and Communication Technology, Bandung Institute of Technology, Ganesa 10, 40132, Bandung, Indonesia
[c] Department of Precision and Microsystems Engineering, Delft University of Technology, Delft, 2628 CD, the Netherlands
[d] Eindhoven University of Technology, PO Box 513, Eindhoven, 5600 MB, the Netherlands

ARTICLE INFO

Keywords:
Sound radiation
Sound transmission
Building component
Time-domain
Discontinuous Galerkin method

ABSTRACT

This study presents numerical solutions for two vibroacoustic problems using the time-domain nodal discontinuous Galerkin (DG) method. The first problem is the impact sound radiation from a rectangular slab into a cuboid room, and the second is the sound transmission between two cuboid rooms with direct and flanking contributions. The structures are modelled as a three-dimensional solid governed by the linear elasticity equations, and sound propagation in the rooms is governed by the linear acoustic equations. In the impact sound radiation case, the normalised sound pressure is evaluated and compared to the one obtained by the modal expansion method. In the sound transmission case, pressure transfer functions between different positions are calculated and compared to those obtained by the finite element method (FEM). The upwind numerical fluxes in DG for both governing equations, as well as the coupling conditions, are presented. There is excellent agreement between the solutions obtained by the nodal DG and those obtained by the modal expansion method/FEM. Although minor discrepancies exist in the resonance frequencies and magnitude, the overall trend shows good agreement.

1. Introduction

Virtual acoustics has undergone significant advancements, enabling users to immerse themselves in an auditory experience closely resembling real-world soundscapes [1,2]. Numerical modelling techniques have become important in achieving a comprehensive and authentic virtual acoustic experience. Despite recent progress in acoustic modelling techniques for virtual acoustics [3–5], the modelling of structural vibrations and acoustic-structure interactions remains underdeveloped. This is especially of high demands in the field of building acoustics, where the understanding of interaction between acoustic waves in air and structural motions of building elements (e.g., walls, floors, windows) is essential for predicting airborne and structure-borne sound transmission and its impact on humans.

There are several models present to predict airborne and structure-borne sound transmission of building elements, including analytical models [6–9] and engineering models [10,11]. However, these models are based on diffuse field assumption [6,10], infinite structure [10], or restricted to simple geometries [6,8,9]. Accurate prediction of sound transmission requires the inclusion of all necessary details such as mechanical properties of structures, boundary conditions, excitation conditions, and so on. To that end, the use of wave-based method is essential.

Wave-based methods solve governing equations of structural vibrations and acoustic wave propagation in the rooms, including their interaction through sound radiation and transmission (vibroacoustic problems). Notably, the finite element method (FEM) and the finite-difference time-domain (FDTD) method have been widely used to model the airborne and structure-borne transmission problems in buildings. For example, FEM was used to model sound transmission between dwellings [12] or double-leaf walls [13–15]. In these works, the acoustic wave equation or modal-bases functions were used to model the sound propagation in air, and thin plate equations [12–14] or three-dimensional solid structure equations [15] were used to model structural vibrations of the walls. Moreover, the wave and finite element method (WFM) has also been used to calculate the transmission loss of thin panels and sandwich panels [16]. On the other hand, the FDTD method was used in Refs. [17,18] to simulate impact sound radiation by using the three-dimensional linear elasticity equations that solved

* Corresponding author at: School of Electrical Engineering and Informatics, Bandung Institute of Technology, Ganesa 10, 40132, Bandung, Indonesia.
E-mail addresses: indra.sihar@itb.ac.id (I. Sihar), Jieun.Yang@tudelft.nl (J. Yang), M.C.J.Hornikx@tue.nl (M. Hornikx).

https://doi.org/10.1016/j.apacoust.2024.110197
Received 28 February 2024; Received in revised form 19 June 2024; Accepted 22 July 2024
Available online 2 August 2024

elastic wave variables for both solid and air domains. In their study, the Lamé's second parameter was set to zero in the air domain to model sound propagation.

The time-domain discontinuous Galerkin (DG) method has emerged as a promising wave-based approach for vibroacoustic problems. This method has advantages compared to the other wave-based method in that (i) it can represent the problem domain using unstructured mesh to deal with a complex domain accurately, (ii) it allows for refinement of the solution by increasing the polynomial order or element number, and (iii) it allows for significantly accelerated calculations [19], since it uses an element-wise formulation to solve the governing equations. Thus, it provides a framework well suited for parallel computation, as well as for local time-stepping [20]. The DG method has recently been advanced in acoustic modelling [21–24] and structural vibration [25,26], however, it is a relatively new method applied to vibroacoustic problems. While the DG method has been studied for fluid-structure problems [27–30] in seismology, to the authors' knowledge, the DG method has never been applied to sound transmission and radiation problems where the fluid and structure have finite dimensions.

This paper presents the implementation of the DG method for sound transmission and radiation in building acoustics applications where the exact numerical fluxes for acoustic waves are derived and coupled with fluxes from elastic waves [26]. This work contributes to the application and validation of the DG method for building acoustic problems paving the way for an accelerated wave-based method. We consider two vibroacoustic problems: (i) impact sound radiation from a rectangular slab into a cuboid room and (ii) sound transmission between two cuboid rooms with direct and flanking contributions. The governing equations and the nodal DG formulation to solve these equations will be given, as well as the methodology to couple the two media using the numerical fluxes. The simulation results are compared with the frequency domain results obtained by the modal expansion method or the FEM solution. Moreover, the appendices present the details of the upwind fluxes for both equations and the modal expansion method used to obtain the analytical solution of the impact sound radiation. The remainder of this paper is organized as follows. In Section 2, the linear elasticity equations and the linear acoustic equations are presented. The nodal DG formulation to solve these equations is given, as well as the methodology to couple the two media using the numerical fluxes. Section 3 describes the example cases in detail. In Section 4, the simulation results for the first problem are compared with the results obtained by the modal expansion method, and the solution for the second problem is compared to the FEM solution. Finally, conclusions of the paper are given in Section 5.

2. Methodology

To solve vibroacoustic problems in this study, the nodal DG method is used and implemented in an in-house Matlab solver. The vibration of structure is modelled by the linear elasticity equations, and sound propagation in air is modelled by the linear acoustic equations. In this section, each set of equations is presented along with the methodology to solve them using the nodal DG method. To couple the two sets of governing equations, the continuity conditions between two subdomains are treated with the numerical flux presented in Section 2.4.

2.1. Linear acoustic equations

The propagation of sound in a room with no wind and constant temperature is governed by the linear acoustic equations. They are derived from the general conservation laws and the adiabatic process of the ideal gas [31,32]. For Cartesian 3-D coordinates, these equations can be written as:

$$\frac{\partial \boldsymbol{q}_a}{\partial t} + \nabla \cdot \boldsymbol{F}(\boldsymbol{q}_a) = \frac{\partial \boldsymbol{q}_a}{\partial t} + \boldsymbol{A}_j \frac{\partial \boldsymbol{q}_a}{\partial x_j} = \boldsymbol{0}, \tag{1}$$

$$\boldsymbol{q}_a(\boldsymbol{x},t) = \begin{bmatrix} u & v & w & p \end{bmatrix}^T,$$

where $\boldsymbol{q}_a$ is the acoustic variable vector with p being the sound pressure, and u, v, w are the velocities in the spatial coordinate vector $\boldsymbol{x} = [x, y, z]$, respectively. The index $j \in [x, y, z]$. The flux matrix reads $\boldsymbol{F}(\boldsymbol{q}_a) = [\boldsymbol{f}_x, \boldsymbol{f}_y, \boldsymbol{f}_z] = [\boldsymbol{A}_x \boldsymbol{q}_a, \boldsymbol{A}_y \boldsymbol{q}_a, \boldsymbol{A}_z \boldsymbol{q}_a]$. The constant flux Jacobian matrix $\boldsymbol{A}_j$ is given as:

$$\boldsymbol{A}_j = \begin{bmatrix} 0 & 0 & 0 & \frac{\delta_{xj}}{\rho_0} \\ 0 & 0 & 0 & \frac{\delta_{yj}}{\rho_0} \\ 0 & 0 & 0 & \frac{\delta_{zj}}{\rho_0} \\ \rho_0 c_0^2 \delta_{xj} & \rho_0 c_0^2 \delta_{yj} & \rho_0 c_0^2 \delta_{zj} & 0 \end{bmatrix}, \tag{2}$$

where ρ_0 is the density of air, and c_0 is the adiabatic sound speed. The δ_{ij} denotes the Kronecker delta function.

2.2. Linear elasticity equations

The linear vibration of a structure can be modelled using the linear elasticity equations, which govern the propagation of elastic waves in a solid medium. This set of equations follows from the momentum conservation and constitutive equations [32]. For a Cartesian 3-D coordinate system, the equations for an isotropic medium can be written as a set of linear first-order hyperbolic equations in a velocity-stress form as:

$$\frac{\partial \boldsymbol{q}_s}{\partial t} + \nabla \cdot \boldsymbol{H}(\boldsymbol{q}_s) = \frac{\partial \boldsymbol{q}_s}{\partial t} + \boldsymbol{B}_j \frac{\partial \boldsymbol{q}_s}{\partial x_j} = \boldsymbol{g} - \boldsymbol{\zeta} \boldsymbol{q}_s, \tag{3}$$

$$\boldsymbol{q}_s(\boldsymbol{x},t) = \begin{bmatrix} u & v & w & \sigma_{xx} & \sigma_{yy} & \sigma_{zz} & \sigma_{xz} & \sigma_{yz} & \sigma_{xy} \end{bmatrix}^T,$$

$$\boldsymbol{g}(\boldsymbol{x},t) = \begin{bmatrix} g_x & g_y & g_z & 0 & 0 & 0 & 0 & 0 & 0 \end{bmatrix}^T,$$

$$\boldsymbol{\zeta} = \mathrm{diag}\begin{pmatrix} \zeta_x & \zeta_y & \zeta_z & 0 & 0 & 0 & 0 & 0 & 0 \end{pmatrix},$$

where $\boldsymbol{q}_s$ is the elastic wave variable vector with u, v, w are the velocities in the x-, y-, and z- directions, respectively. σ_{xx}, σ_{yy}, σ_{zz}, σ_{xz}, σ_{yz}, σ_{xy} are the normal and shear stress components; g_x, g_y, g_z are the body forces (which act as a source in the medium), and $\zeta_x, \zeta_y, \zeta_z$ are the viscous damping forces in the x-, y-, and z- directions, respectively. The flux matrix reads $\boldsymbol{H}(\boldsymbol{q}_s) = [\boldsymbol{h}_x, \boldsymbol{h}_y, \boldsymbol{h}_z] = [\boldsymbol{B}_x \boldsymbol{q}_s, \boldsymbol{B}_y \boldsymbol{q}_s, \boldsymbol{B}_z \boldsymbol{q}_s]$. The constant flux Jacobian matrix $\boldsymbol{B}_j$ is given as:

$$\boldsymbol{B}_j = \left[\begin{array}{c|c} \boldsymbol{0}_{3\times3} & \boldsymbol{B}_{1,j} \\ \hline \boldsymbol{B}_{2,j} & \boldsymbol{0}_{6\times6} \end{array}\right], \boldsymbol{B}_{1,j} = -\frac{1}{\rho}\begin{bmatrix} \delta_{xj} & 0 & 0 & \delta_{zj} & 0 & \delta_{yj} \\ 0 & \delta_{yj} & 0 & 0 & \delta_{zj} & \delta_{xj} \\ 0 & 0 & \delta_{zj} & \delta_{xj} & \delta_{yj} & 0 \end{bmatrix},$$

$$\boldsymbol{B}_{2,j} = -\begin{bmatrix} (\lambda+2\mu)\delta_{xj} & \lambda\delta_{yj} & \lambda\delta_{zj} \\ \lambda\delta_{xj} & (\lambda+2\mu)\delta_{yj} & \lambda\delta_{zj} \\ \lambda\delta_{xj} & \lambda\delta_{yj} & (\lambda+2\mu)\delta_{zj} \\ \mu\delta_{zj} & 0 & \mu\delta_{xj} \\ 0 & \mu\delta_{zj} & \mu\delta_{yj} \\ \mu\delta_{yj} & \mu\delta_{xj} & 0 \end{bmatrix}, \tag{4}$$

where λ and μ are the Lamé parameters, ρ is the solid mass density, and index j has components $[x, y, z]$. The solution of Equation (3) consists of a linear combination of elastic waves propagating with longitudinal wave speed ($c_p = \sqrt{(\lambda+2\mu)/\rho}$) and transverse wave speed ($c_s = \sqrt{\mu/\rho}$). The Lamé parameters are represented by using Young's modulus (E) and Poisson's ratio (ν) as $\lambda = E\nu/(1+\nu)(1-2\nu)$ and $\mu = E/2(1+\nu)$. Equations (1)-(4) are supplemented with initial values as well as boundary conditions (BCs) to complete the problem definition.

2.3. Nodal discontinuous Galerkin method

The nodal discontinuous Galerkin (DG) method is used to solve Equations (1)-(4). The algorithm of the method is developed by Hesthaven and Warburton [33] and is adopted in this study. The problem domain is approximated by the computational domain Ω_h with K number of non-overlapping rectilinear tetrahedral elements D^k as $\Omega_h = \cup_{k=1}^{K} D^k$. The problem domain consists of the structural subdomain (Ω_h^s) and the air

subdomain (Ω_h^a) where $\Omega_h = \Omega_h^s \cup \Omega_h^a$. The subscript h denotes the approximation of the real physical domain. On each D^k, the local solution is expanded by a combination of nodal basis functions as:

$$\boldsymbol{q}_{sh}^k(\boldsymbol{x},t) = \sum_{i=1}^{N_p} \boldsymbol{q}_{sh}^k(\boldsymbol{x}_i^k,t) l_i^k(\boldsymbol{x}), \tag{5}$$

$$\boldsymbol{q}_{ah}^k(\boldsymbol{x},t) = \sum_{i=1}^{N_p} \boldsymbol{q}_{ah}^k(\boldsymbol{x}_i^k,t) l_i^k(\boldsymbol{x}), \tag{6}$$

where $\boldsymbol{q}_{sh}^k(\boldsymbol{x}_i^k,t)$, $\boldsymbol{q}_{ah}^k(\boldsymbol{x}_i^k,t)$ are the unknown nodal values of the elastic and acoustic wave variables, respectively. $l_i^k(\boldsymbol{x})$ are the 3-D Lagrange interpolation polynomials based on the nodal points $\boldsymbol{x}_i$, and N_p is the number of nodal points. The global solutions are approximated as the direct sum of the local solutions as:

$$\boldsymbol{q}_s(\boldsymbol{x},t) \approx \boldsymbol{q}_{sh}(\boldsymbol{x},t) = \oplus_{k=1}^K \boldsymbol{q}_{sh}^k(\boldsymbol{x},t), \tag{7}$$

$$\boldsymbol{q}_a(\boldsymbol{x},t) \approx \boldsymbol{q}_{ah}(\boldsymbol{x},t) = \oplus_{k=1}^K \boldsymbol{q}_{ah}^k(\boldsymbol{x},t). \tag{8}$$

The closed expression of the Lagrange interpolation polynomials in tetrahedral elements is constructed by the products of the Jacobi polynomials of order N, and the distribution of nodal points follows the optimised Legendre-Gauss-Lobato (LGL) points over a tetrahedral element as presented in Ref. [33]. The number of nodal points per element is $N_p = (N+1)(N+2)(N+3)/6$.

For each element in solid domain Ω_h^s, the nodal basis functions are used to approximate the elastic wave variables and the body forces in Equation (3). Then the residuals of the approximations are multiplied by the test functions following the Galerkin method. By performing spatial integration by parts twice, the strong formulation of Equation (3) is as follows:

$$\begin{aligned}\int_{D^k} \left[\frac{\partial \boldsymbol{q}_{sh}^k}{\partial t} + \nabla \cdot \boldsymbol{H}(\boldsymbol{q}_{sh}^k)\right] l_i^k \mathrm{d}\boldsymbol{x} = &\int_{D^k} (\boldsymbol{g}_h^k - \boldsymbol{\zeta} \boldsymbol{q}_{sh}^k) l_i^k \mathrm{d}\boldsymbol{x} \\ &- \int_{\partial D^k} \boldsymbol{n} \cdot \left[\boldsymbol{H}^* - \boldsymbol{H}(\boldsymbol{q}_{sh}^k)\right] l_i^k \mathrm{d}\boldsymbol{x},\end{aligned} \tag{9}$$

where ∂D^k is the element surface, $\boldsymbol{g}_h^k$ is the approximated body force vector, and $\boldsymbol{n} = [n_x, n_y, n_z]$ is the outward normal vector of the element surface ∂D^k. The flux along the normal direction of the element surface is defined as $\boldsymbol{n} \cdot \boldsymbol{H} = (n_x \boldsymbol{h}_x + n_y \boldsymbol{h}_y + n_z \boldsymbol{h}_z)$, and the $\boldsymbol{H}^*$ is the numerical flux.

The numerical flux ensures continuity of the global solution. It is a function of the interior solution ($\boldsymbol{q}_{sh}^-$), which is the solution within the element D^k, and the exterior solution ($\boldsymbol{q}_{sh}^+$), which is the solution of the neighbouring elements around D^k. In this work, the upwind numerical flux is chosen as the numerical flux. The upwind numerical flux can be derived by solving the Riemann problem at the interface between two homogeneous media. This interface represents the faces of two neighbouring elements located at the same position. Consider that the interface lies at $\boldsymbol{x} = 0$. The properties of the medium $(\lambda^-, \mu^-, \rho^-)$ are those of the internal medium for $\boldsymbol{x} < 0$, and $(\lambda^+, \mu^+, \rho^+)$ are those of the adjacent one for $\boldsymbol{x} > 0$. The Riemann problem is a discontinuous initial value problem that happens at this interface as:

$$\boldsymbol{q}_{sh}(\boldsymbol{x},0) = \begin{cases} \boldsymbol{q}_{sh}^- & \text{if } \boldsymbol{x} < 0, \\ \boldsymbol{q}_{sh}^+ & \text{if } \boldsymbol{x} > 0. \end{cases} \tag{10}$$

The solution to this problem, the intermediate solution ($\boldsymbol{q}_{sh}^*(\boldsymbol{0},t)$), is derived using the Rankine-Hugoniot jump condition as described in Refs. [25], [29], [32]. The numerical fluxes $\boldsymbol{n} \cdot \boldsymbol{H}^* = \boldsymbol{n} \cdot \boldsymbol{H}(\boldsymbol{q}_{sh}^*)$ are a function of the intermediate solution. After defining the numerical flux, the nodal basis and numerical flux are substituted into Equation (9) to obtain the semi-discrete form. The details of this elastic wave equation semi-discrete form can be found in Ref. [26].

For each element in the air subdomain Ω_h^a, the same methodology as above are used. The nodal basis functions are used to approximate the sound wave variables in Equation (1). This leads to its strong formulation as:

$$\int_{D^k} \left[\frac{\partial \boldsymbol{q}_{ah}^k}{\partial t} + \nabla \cdot \boldsymbol{F}(\boldsymbol{q}_{ah}^k)\right] l_i^k \mathrm{d}\boldsymbol{x} = -\int_{\partial D^k} \boldsymbol{n} \cdot \left[\boldsymbol{F}^* - \boldsymbol{F}(\boldsymbol{q}_{ah}^k)\right] l_i^k \mathrm{d}\boldsymbol{x}. \tag{11}$$

The flux along the normal direction of the element surface is defined as $\boldsymbol{n} \cdot \boldsymbol{F} = (n_x \boldsymbol{F}_x + n_y \boldsymbol{F}_y + n_z \boldsymbol{F}_z)$, and the $\boldsymbol{F}^*$ is the numerical flux for the sound wave variables. The upwind numerical flux is also used for the linear acoustics equations. Different from the elastic medium, air has interior medium properties that consist of (ρ_0^-, c_0^-) and (ρ_0^+, c_0^+) for the exterior one. The details on the numerical flux for wave propagation in air are given in Appendix A. After defining the numerical flux, the nodal basis and the numerical flux are substituted into Equation (9) to obtain the semi-discrete form for each element as:

$$\begin{aligned}
\boldsymbol{M}^k \frac{\partial \boldsymbol{u}_h^k}{\partial t} + \frac{1}{\rho_0} \boldsymbol{S}_x^k \boldsymbol{p}_h^k &= -\sum_{r=1}^4 \boldsymbol{M}^{kr} \hat{\boldsymbol{F}}_u^{kr}, \\
\boldsymbol{M}^k \frac{\partial \boldsymbol{v}_h^k}{\partial t} + \frac{1}{\rho_0} \boldsymbol{S}_y^k \boldsymbol{p}_h^k &= -\sum_{r=1}^4 \boldsymbol{M}^{kr} \hat{\boldsymbol{F}}_v^{kr}, \\
\boldsymbol{M}^k \frac{\partial \boldsymbol{w}_h^k}{\partial t} + \frac{1}{\rho_0} \boldsymbol{S}_z^k \boldsymbol{p}_h^k &= -\sum_{r=1}^4 \boldsymbol{M}^{kr} \hat{\boldsymbol{F}}_w^{kr}, \\
\boldsymbol{M}^k \frac{\partial \boldsymbol{p}_h^k}{\partial t} + \rho_0 c_0^2 \boldsymbol{S}_x^k \boldsymbol{u}_h^k + \rho_0 c_0^2 \boldsymbol{S}_y^k \boldsymbol{v}_h^k + \rho_0 c_0^2 \boldsymbol{S}_z^k \boldsymbol{w}_h^k &= -\sum_{r=1}^4 \boldsymbol{M}^{kr} \hat{\boldsymbol{F}}_p^{kr},
\end{aligned} \tag{12}$$

$\boldsymbol{u}_h^k$, $\boldsymbol{v}_h^k$, $\boldsymbol{w}_h^k$, and $\boldsymbol{p}_h^k$ are vectors representing all sound wave variables at the nodal points $\boldsymbol{x}_i$, with $i = 1$ to N_p. The terms $\hat{\boldsymbol{F}}_u^{kr}$, $\hat{\boldsymbol{F}}_v^{kr}$, $\hat{\boldsymbol{F}}_w^{kr}$, and $\hat{\boldsymbol{F}}_p^{kr}$ are the flux terms associated with the term $\boldsymbol{n} \cdot \left[\boldsymbol{F}^* - \boldsymbol{F}(\boldsymbol{q}_{ah}^k)\right]$ over the element surface in Equation (11). The element mass matrix ($\boldsymbol{M}^k$), the element stiffness matrices ($\boldsymbol{S}_x^k, \boldsymbol{S}_y^k, \boldsymbol{S}_z^k$), and the element face matrix ($\boldsymbol{M}^{kr}$), the details on these matrices are given in Refs. [21,33]. Afterwards, the semi-discrete form can be expressed in the form of ordinary differential equations as:

$$\frac{\mathrm{d}\boldsymbol{q}_{sh}}{\mathrm{d}t} = \boldsymbol{\mathcal{L}}_s\left(\boldsymbol{q}_{sh}(t), t\right), \tag{13}$$

$$\frac{\mathrm{d}\boldsymbol{q}_{ah}}{\mathrm{d}t} = \boldsymbol{\mathcal{L}}_a\left(\boldsymbol{q}_{ah}(t), t\right), \tag{14}$$

where $\boldsymbol{q}_{sh}$, $\boldsymbol{q}_{ah}$ are the vector of all nodal solutions, and $\boldsymbol{\mathcal{L}}_s$, $\boldsymbol{\mathcal{L}}_a$ are the semi-discrete operator conducted over all elements in the solid and in air, respectively. Finally, various methods can be used to integrate the time derivative in Equations (13)-(14). In this work, the fourth-order Runge-Kutta method with eight stages (RKF84) is used, which is described in Ref. [34]. The time-step (Δt) for the time integration is defined as:

$$\Delta t = \frac{C_{CFL} \cdot \min(r_{D^k})}{N^2 \cdot \max(c_p)}, \tag{15}$$

where C_{CFL} is the Courant number, $\max(c_p)$ is the maximum longitudinal wave speed, and $\min(r_{D^k})$ is the shortest element edge in the computational domain. It should be pointed out that Δt is determined by the fastest wave on the whole domain, which in this case is the elastic longitudinal wave. To complete the numerical formulation, the BCs, force excitation, and initial values should be given. The methodology to apply the force excitation and the BCs for the structure subdomain can be found in Ref. [25], while the BCs treatment for the air subdomain can be found in Ref. [21].

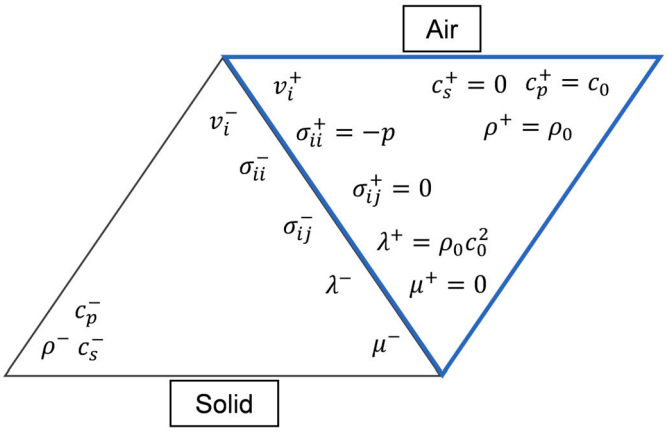

Fig. 1. The jump conditions on the interface between solid and air.

2.4. Interface between solid and air

The interaction between solid and air is represented by the perfect slip boundary condition. In this condition, the shear stress has to vanish, while the continuity of the normal stresses and velocities has to be guaranteed [27]. In the nodal DG method, this can be constructed through the numerical fluxes. In order to realise this, the mesh must conform to the discontinuity between solid and air. It means that the element interfaces must be aligned with the material interface.

In the structural elements interfaces, the numerical fluxes are computed following Ref. [26], with the exterior values of each variable set as illustrated in Fig. 1. The air (exterior element) is assumed to be an inviscid fluid, where the fluid cannot sustain any shear stress. Thus, the transversal wave speed in the air c_s^+ is zero, and the shear stresses are set as $\sigma_{ij}^+ = 0$. Moreover, the exterior values of density and longitudinal wave speed are $\rho^+ = \rho_0$ and $c_p^+ = c_0$ following medium properties of air. The exterior value of the first Lamé parameter is set as the bulk modulus of air, $\lambda^+ = \rho_0 c_0^2$, and the exterior second Lamé parameter (shear modulus) is set to zero, $\mu^+ = 0$.

To maintain the continuity of the velocities, the coupling can be set directly since the same variables exist both in air and solid material. The exterior velocity of the solid element, v_i^+, equals the velocity in the air element and vice versa. Moreover, the normal stresses are set by the condition $\sigma_{ij} n_j = -p n_j$ such as presented in Ref. [35], and since shear stresses in air are zero, the normal stresses in the solid are equal to sound pressure in air as $\sigma_{xx}^+ = \sigma_{yy}^+ = \sigma_{zz}^+ = -p$. This methodology is also found in Refs. [27,32].

3. Case studies

In this study, three vibro-acoustic cases are simulated using the nodal DG method. The three cases are the sound radiation of a concrete slab into a room, sound transmission between two rooms through a single separating wall, and sound transmission between two rooms with flanking contributions. The first and second cases are compared with the analytical solution and the finite element method solution for the acoustic-solid interaction problem. These cases are chosen to show the validity of the nodal DG methodology for vibro-acoustic problems. The third case is given to demonstrate the difference between sound transmission values of a wall with and without flanking paths.

3.1. Impact sound radiation

The first case concerns impact sound radiation from a concrete slab into a room, as shown in Fig. 2a. The slab only radiates the sound towards the room, where the upper surface does not radiate the sound. The room and the slab have dimensions [1.2 m × 0.8 m × 1 m] and [1.2 m × 0.8 m × 0.08 m], respectively. The slab has simply supported BCs on the edges and free BCs on the top. The room has rigid BCs on all surfaces.

The mechanical properties of the concrete slab are as follows: Young's modulus $E = 13.6$ GPa, density $\rho = 2300\,\mathrm{kg/m^3}$, and Poisson's ratio $\nu = 0.3$. Air has a density of $\rho_0 = 1.2\,\mathrm{kg/m^3}$ and a wave speed of $c_0 = 344\,\mathrm{m/s}$. An impact force on the slab at position $F = [0.2, 0.64, 1.08]\,\mathrm{m}$ (marked with blue dot) is given as:

$$g_z(t) = -\left(a_2 + a_1(t - t_d)^2\right) e^{a_1 (t - t_d)^2}, \tag{16}$$

with centre time $t_d = 7\,\mathrm{ms}$, centre frequency $f_c = 500\,\mathrm{Hz}$, $a_1 = -(\pi f_c)^2$, and $a_2 = 0.5$. The methodology to excite the point force can be seen in Ref. [25] and is adopted for this work. The impact point force is positioned close to a corner of the plate to reduce the possibility of hitting at multiple nodal lines of the slab at lower order modes. The simulation duration is 4 seconds, and three receivers are distributed along the room diagonal at $R1 = [0.2, 0.2, 0.25]\,\mathrm{m}$, $R2 = [0.6, 0.4, 0.5]\,\mathrm{m}$, $R3 = [1, 0.6, 0.75]\,\mathrm{m}$ to obtain the sound radiation from slab as shown in Fig. 2a (marked by red dots).

To discretise the problem domain for the nodal DG method, the mesh generator of COMSOL Multiphysics is used [36]. The mesh is shown in Fig. 2b. It consists of 241 and 452 tetrahedral elements to represent the concrete slab and the room, respectively. For the computation with the DG method, the Lagrange interpolation polynomials with an order of $N = 4$ are applied. With this polynomial order, the room has 10 degrees of freedom per wavelength (DPW) at 850 Hz, which becomes the upper-frequency limit. Moreover, the material properties of the concrete slab determine the time step since the solid medium has a much faster longitudinal wave speed than air ($c_p = 2821.3$ m/s). The Courant number $C_{CFL} = 1$ is selected, resulting in $\Delta t = 1.5588 \cdot 10^{-6}$ s. The elastic longitudinal wavelength at 850 Hz is 3.32 m, which means that the slab has a DPW number of 158.9. Note that the slab's length is much shorter than the wavelength, and the thickness of the slab controls the discretisation to ensure a good element skewness.

The nodal DG solution is then compared with the analytical solution based on the modal expansion method to validate the current computation. The time-domain sound pressure in each receiver and the force are converted into the frequency-domain data using the Fast Fourier transform. In doing FFT, the initial two seconds of simulated data are not tapered or windowed. The signal is then tapered over the next 2 seconds using half part of the Hann window with 2 second duration. This tapering is done to prevent the Gibbs effect while also having a minimum decay in the signal. Having the frequency-domain data, the normalised sound pressure or the transfer function is calculated as:

$$P_n(\boldsymbol{x}, f) = \frac{P(\boldsymbol{x}, f)}{G(F, f)}, \tag{17}$$

where $P(\boldsymbol{x}, f)$ is the frequency-domain pressure at each receiver location, and $G(F, f)$ is the frequency-domain force. For the reference solution, the modal expansion solution is obtained in frequency-domain, and the vibration of the slab is modelled by using the first shear deformation theory (FSDT) (see Appendix B for more details).

3.2. Sound transmission

3.2.1. Direct sound transmission

The second case is sound transmission between two rooms through a single concrete panel where flanking transmission is not included. The case geometry can be seen in Fig. 3a, where the source room is the one closest to the coordinate origin. The source and receiver rooms have dimensions of [3.2 m × 2.9 m × 2.4 m] and [2.7 m × 2.9 m × 2.4 m], respectively. The panel (marked by grey surfaces) has a thickness of 0.2 m, with all edges having fixed BCs. The red rectangle indicates the location of the sound source (Q), the blue dots mark the receivers in the source room (S1-S3), and the black dots mark the receivers in

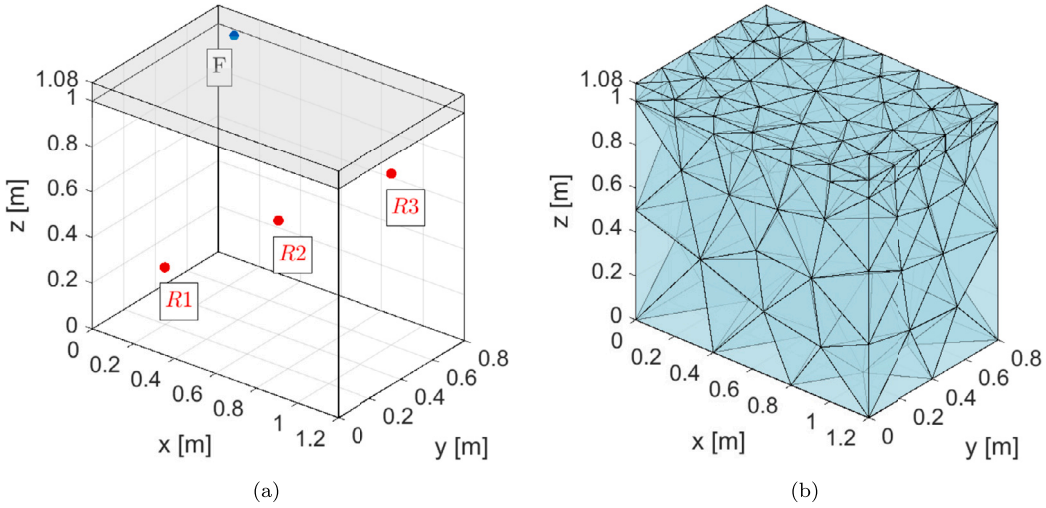

Fig. 2. (a) The impact sound radiation case with the force and receiver positions, and (b) its mesh for the DG method computation.

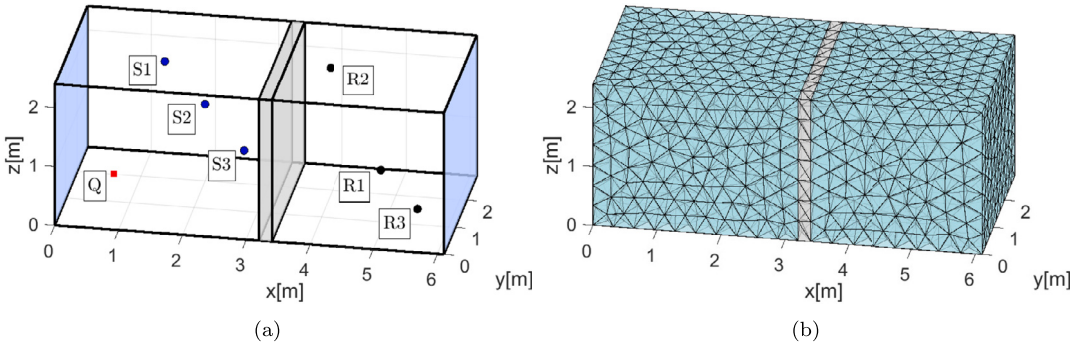

Fig. 3. (a) The sound transmission through a single concrete panel case, and (b) its mesh for the DG method computation.

Table 1
Locations of the source and receivers for the single panel transmission case.

Index	(x, y, z) [m]
Q	(0.8, 0.725, 0.6)
S1	(1.3, 2.4, 1.8)
S2	(2, 2, 1.3)
S3	(2.7, 1.5, 0.8)
R1	(4.8, 1.8, 0.5)
R2	(3.9, 2.4, 1.9)
R3	(5.6, 0.5, 0.5)

the receiver room (R1-R3). The locations of these points are shown in Table 1.

The properties of the concrete slab and air are the same as in the case of impact sound radiation (see Section 3.1). In addition, viscous damping forces $\zeta_x = \zeta_y = \zeta_z = 20\,[N \cdot kg/m^3]$ are added to the concrete to dissipate the vibration energy during transmission. Frequency-independent impedance BCs are applied to the surfaces of the rooms indicated by blue surface in Fig. 3a, and each surface has a real-valued reflection coefficient of $R = 0.95$. Other surfaces in the room are set as rigid BCs. The simulation duration is 2 seconds, and to excite the sound on the location Q, initial values are given as:

$$p(\boldsymbol{x}, t=0) = Q_0 \cdot \mathrm{e}^{\frac{-ln(2)}{b^2}\left((x-x_q)^2+(y-y_q)^2+(z-z_q)^2\right)},$$

$$\boldsymbol{v}(\boldsymbol{x}, t=0) = \boldsymbol{0}.$$

This is a pressure Gaussian pulse centred at the source coordinates (x_q, y_q, z_q), with pulse half-bandwidth $b = 0.15$ and amplitude of $Q_0 = 10$ Pa.

The mesh for the nodal DG method is shown in Fig. 3b, where the concrete panel has 531 elements, and both rooms have a total of 16516 elements. The Lagrange interpolation polynomial order is $N = 3$. With these values, the solution has approximately 10 DPW at 650 Hz, which is the upper frequency limit for the current configuration. The Courant number $C_{CFL} = 1$ is selected, resulting in $\Delta t = 6.4403 \cdot 10^{-6}$ s. The methodology of applying the frequency-independent impedance BCs for the nodal DG method can be found in Ref. [21].

To evaluate the numerical accuracy of the nodal DG method solution, the difference between the sound pressure level (ΔL_p) obtained in the source room ($L_p^S(\boldsymbol{x})$) and the one obtained in the receiver room ($L_p^R(\boldsymbol{x})$) is calculated as:

$$\Delta L_p = L_p^S(\boldsymbol{x}) - L_p^R(\boldsymbol{x}). \tag{18}$$

Three values of ΔL_p are calculated, i.e., the ΔL_p between S1 and R1, S2 and R2, and between S3 and R3. These ΔL_p values are then compared with the values obtained by FEM.

The FEM solutions are obtained by COMSOL Multiphysics 5.4 [36]. In COMSOL, the acoustic-solid interaction solver in the frequency-domain is used. In this solver, the acoustic wave equations and the elastic wave equations are solved for the 3-D geometry. The two-way coupling includes the acoustic pressure load on the structure and the structural acceleration as experienced by the air. The room is discretised using tetrahedral elements, and quadratic basis functions are used. The size of elements is at maximum 10 cm, which is approximately one-fifth of minimum acoustic wavelength, $\lambda_{min}/5$. In FEM, a point source is used to represent the sound excitation in the source room, and surface impedance BC is applied to the walls coloured in blue in Fig. 3a as $Z_{wall} = Z_{air} \cdot (1+R)/(1-R)$.

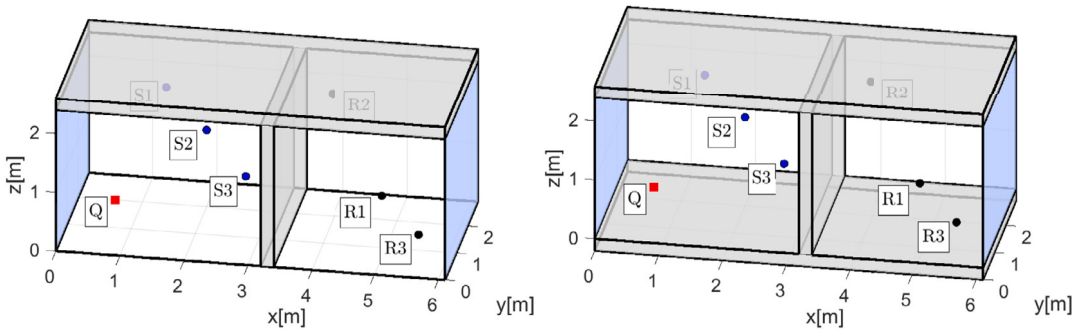

Fig. 4. Sound transmission in rooms with flanking contribution, for case (a) via ceiling and (b) via ceiling and floor.

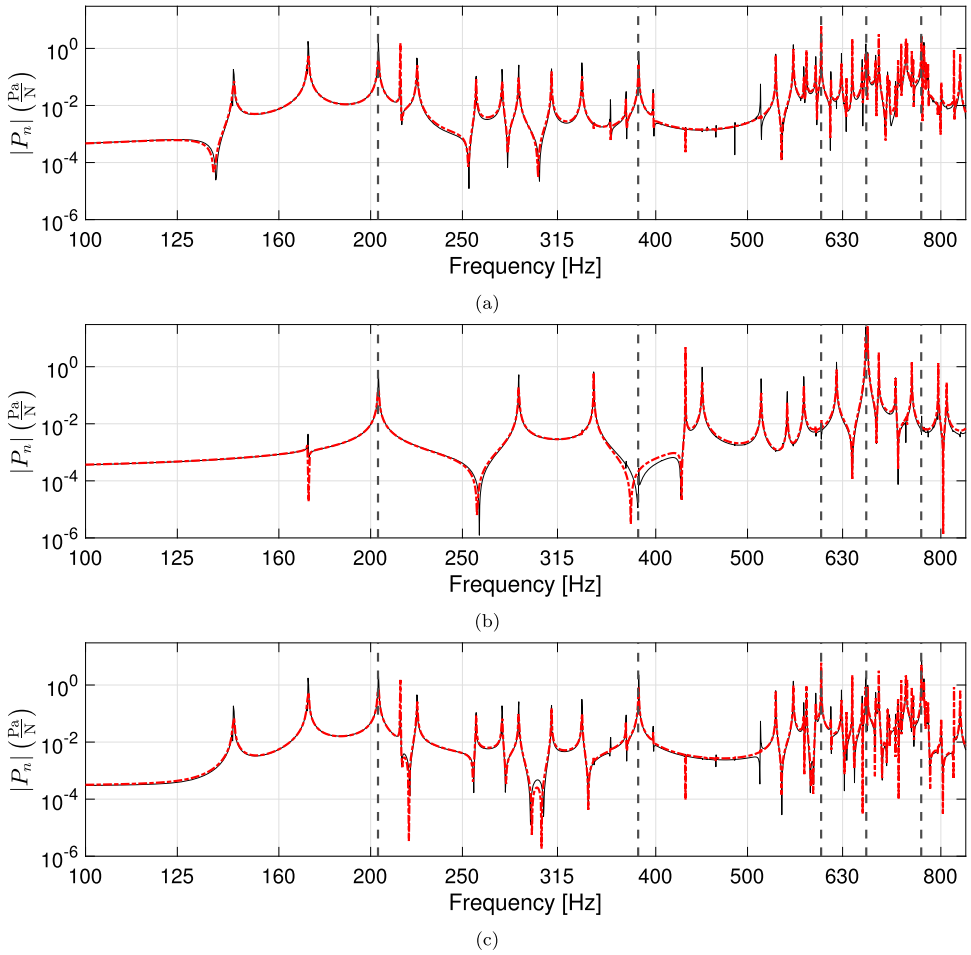

Fig. 5. The normalised sound pressure for the impact sound radiation case at position (a) R1, (b) R2, and (c) R3. Black lines represent the nodal DG results, red dashed lines represent the modal expansion results, and the black dashed vertical lines represent the locations of slab's natural frequencies based on FSDT.

3.2.2. Sound transmission with flanking contribution

The third case is an extension of the single panel case from Section 3.2.1, where the top and bottom slabs of the building are included. These inclusions add flanking transmission contributions as shown in Fig. 4. The first configuration is via the ceiling, and the second is via ceiling and floor. These configurations are simulated with the nodal DG method to show the differences in transfer functions compared to the single panel configuration. The cases are given to demonstrate the ability of the nodal DG method to simulate building acoustic problems. The computational settings and material properties of these two configurations are the same as for the case with a single panel, as in Section 3.2.1. The number of elements in the rooms are slightly changed due to the inclusion of the ceiling and floor. The flanking configuration via ceiling has 1845 elements for the solid structure and 16724 elements for the air, while the one via ceiling and floor has 3210 elements for the solid structure and 16578 for the air.

4. Results and discussions

4.1. Impact sound radiation

Figs. 5a-5c show the magnitudes of the normalised sound pressure at different receivers obtained by the nodal DG and modal expansion methods. As can be seen, the results are in excellent agreement. Accord-

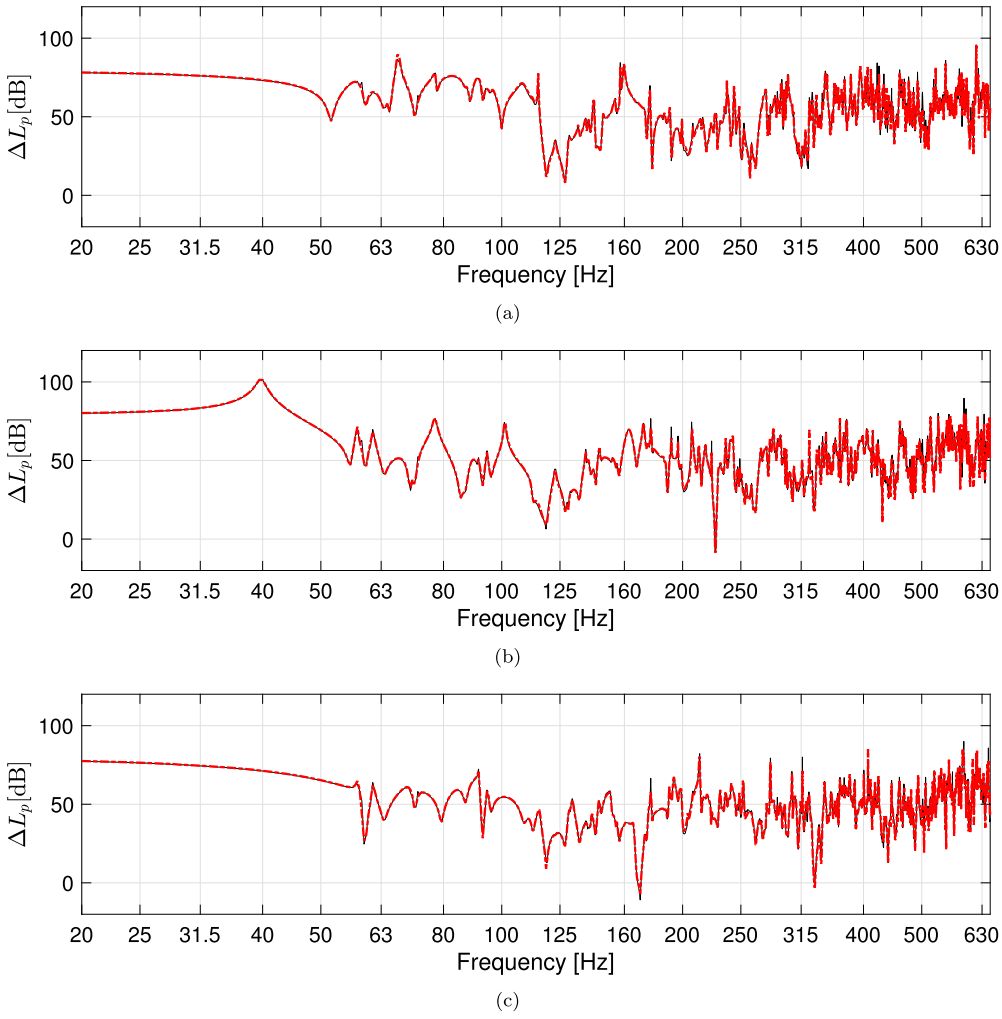

Fig. 6. The ΔL_p between position (a) S1 and R1, (b) S2 and R2, and (c) S3 and R3 for the direct transmission case. Black lines represent ΔL_p obtained by the nodal DG and red dashed lines represent ΔL_p obtained by FEM.

Table 2
Natural frequencies of the concrete slab obtained from FSDT. The m_1, m_2 indicates the number of the anti-node in the x-, and y- directions. (see Appendix B).

Modal index (m_1, m_2)	Natural Frequency [Hz]
1,1	203.6
2,1	383.3
1,2	598.0
3,1	667.3
2,2	762.7

ing to FSDT, there are five natural frequencies below 850 Hz in the slab. These frequencies are indicated by vertical lines in the figures and listed in Table 2. The natural frequencies of the slab are well separated within the frequency range of interest. While for the room, ninety natural frequencies exist below 850 Hz, assuming that the room has rigid BCs.

The natural frequencies of the room mainly characterise the spectrum of the impact sound in the room since the room has more natural frequencies. There are minor discrepancies between the nodal DG and modal expansion solutions, especially in the magnitude and location of the peaks (local maxima) and dips (local minima) of the normalised pressure. For instance, at receiver R2 (which is located exactly in the middle of the room) at 383 Hz and receiver R3 at around 300 Hz. Both solutions have no damping in the configuration, which might lead to different magnitudes at these locations. Moreover, the modal expansion solution is based on the FSDT theory instead of the linear elasticity equation, which could account for some discrepancies.

4.2. Sound transmission

The sound pressure level difference (ΔL_p) values between two rooms divided by a single panel are presented in Figs. 6a-6c. It can be seen that the results obtained by the nodal DG method and FEM are in a very good agreement. Minor discrepancies occur in the peak of ΔL_p values, but the overall trends of the three ΔL_p agree very well with the FEM solution. It can be seen that above 250 Hz the room acoustic modal density is high, with the peaks of the ΔL_p close to each other. The number of acoustic modes in each frequency band is given in Table 3 assuming that all surfaces are rigid. Due to this high number of modes, it is clearer to present the results in 1/3 octave frequency bands.

Now, the ΔL_p values between the single panel to the panels with flanking transmission contribution (via ceiling and ceiling and floor) are presented. The ΔL_p of different locations are shown in Figs. 7a-7c. It can be seen that the single panel has a higher ΔL_p at almost all frequency bands compared to the two scenarios that include flanking transmission. This means that the addition of ceiling and floor increases the overall transmitted sound energy from the source room to the receiver room.

The critical frequency of the concrete panel can be obtained as $f_c = c_0/(1.8 \cdot c_p h) = 116.5$ Hz, where c_0, c_p and h are the sound wave velocity in air, the longitudinal elastic wave velocity and the panel thickness, respectively. Due to this frequency, the ΔL_p values at the 125 Hz

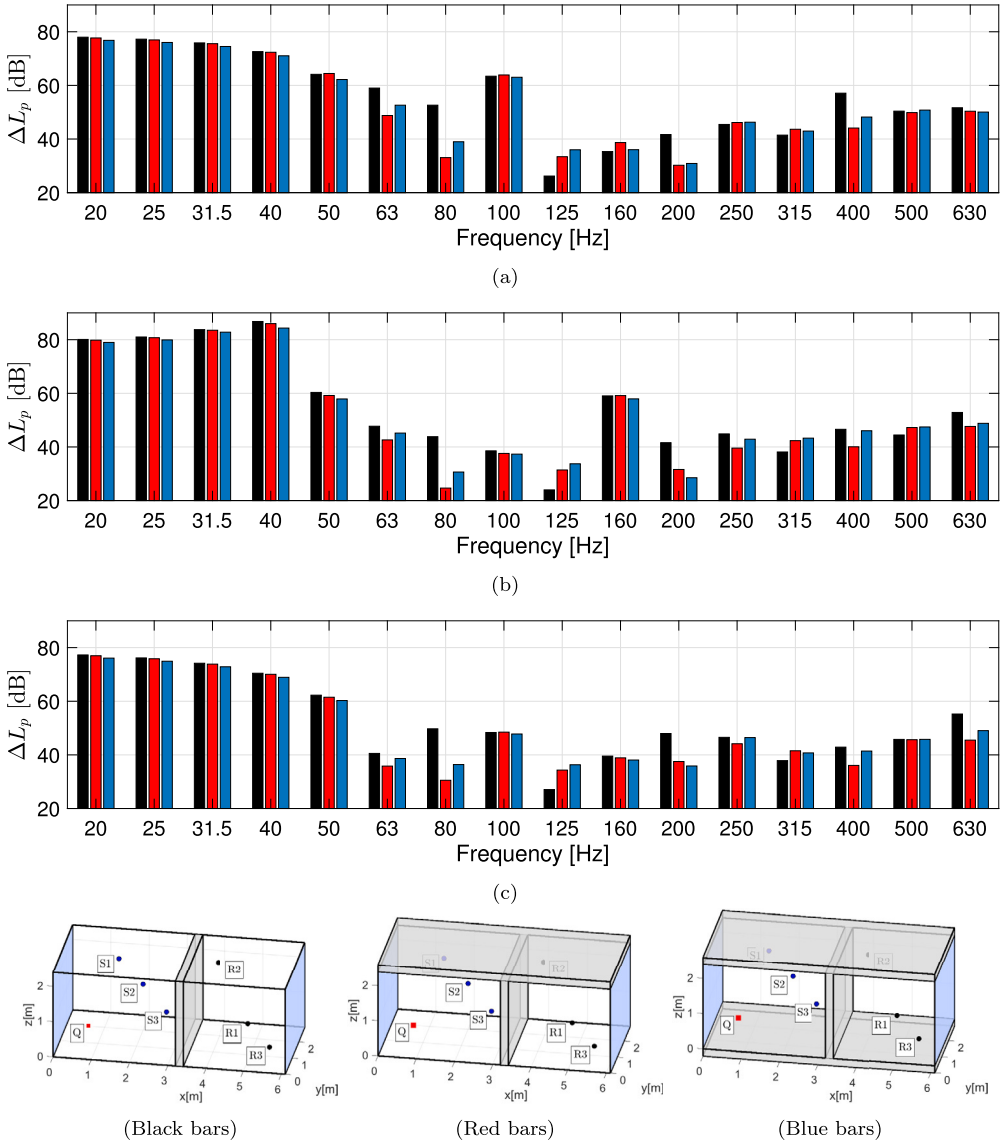

Fig. 7. One-third octave band sound pressure level difference between position (a) S1 and R1, (b) S2 and R2, and (c) S3 and R3. Black bars refer to the single panel with only direct transmission path, red bars refer to the panel with flanking transmission via the ceiling, and blue bars refer to the panel with flanking transmission via ceiling and floor.

Table 3
Number of the acoustic modes of the source and receiver rooms with all room surfaces are assumed rigid.

1/3 octave band centre frequency [Hz]	Number of modes [-]	
	Source room	Receiver room
50	1	0
63	2	2
80	1	2
100	4	2
125	5	6
160	13	9
200	19	15
250	33	32
315	66	57
400	126	110
500	154	156
630	314	224

1/3 octave band are quite low for all panel configurations, especially for the single panel configuration. The figures also show that for the configuration of flanking transmission via ceiling, the ΔL_p values at 80 Hz are lower compared to other configurations. These might caused by the strong coupling between the ceiling vibration to the sound in the rooms.

5. Conclusions

This paper presented a methodology to solve vibroacoustic problems (represented by linear acoustic and elasticity equations) using the nodal DG method. The coupling conditions between acoustic and elastic wave variables provided by upwind fluxes are described. By incorporating this method into the modelling framework, we aim to provide a more comprehensive understanding of vibroacoustic phenomena paving the way for accelerated DG simulations for vibroacoustic problems, facilitating the development of more accurate and realistic virtual acoustic environments. The comparison of the impact sound radiation of a concrete slab into a room calculated using the nodal DG method and an analytical method shows a good agreement. There are slight discrepancies in the locations and magnitudes of natural frequencies. For a transmission case, comparing the transfer functions between receiver locations in two rooms divided by a single concrete wall as computed with the DG method and a reference solution using the FEM shows al-

most identical results. Moreover, when flanking transmission exists, the critical frequency of concrete panels is affecting the ΔL_p values between rooms. The results show variations in transfer functions due to flanking paths, requiring analysis of configurations to predict these variations. Numerical models can be more efficient than experimental methods for predicting these variations. One drawback of the current methodology is the small time step (Δt), which is determined by the elastic wave-speed in the structure. In further work, utilising a multi-time or a local time-stepping methodology could improve the computational performance of the nodal DG method for vibroacoustic applications. Once this is accomplished, this method would be a very powerful approach to address engineering building acoustics problems at low frequencies where solutions of the full governing equations are required.

CRediT authorship contribution statement

Indra Sihar: Writing – review & editing, Writing – original draft, Visualization, Validation, Software, Methodology, Investigation, Funding acquisition, Formal analysis, Data curation, Conceptualization. **Jieun Yang:** Writing – review & editing, Writing – original draft, Supervision, Formal analysis. **Maarten Hornikx:** Writing – review & editing, Writing – original draft, Supervision, Resources, Funding acquisition, Formal analysis.

Declaration of competing interest

The authors declare the following financial interests/personal relationships which may be considered as potential competing interests: Indra Sihar reports financial support was provided by Bandung Institute of Technology, Dana Program Dosen Tidak Tetap Peneliti LPIT-ITB Tahun 2024 nomor 299/IT1.B07.5/TA.00/2024. Indra Sihar reports financial support was provided by Ministry of Finance of Republic of Indonesia under the framework of endowment fund for education (LPDP), grant: scholarship reference number S-3158/LPDP.3/2014. If there are other authors, they declare that they have no known competing financial interests or personal relationships that could have appeared to influence the work reported in this paper.

Data availability

Data will be made available on request.

Acknowledgement

The first author is funded by Dana Program Dosen Tidak Tetap Peneliti LPIT-ITB Tahun 2024 nomor 299/IT1.B07.5/TA.00/2024. This work is also partially supported by the Ministry of Finance of the Republic of Indonesia under the framework of endowment fund for education (LPDP), scholarship reference number S-3158/LPDP.3/2014.

Appendix A. Upwind fluxes for linear acoustic equations

The upwind numerical flux for acoustic wave propagation ($\boldsymbol{n}\cdot\boldsymbol{H}^*$) is presented here. The methodology for obtaining this flux based on the Rankine-Hugoniot jump condition can be found in Ref. [32]. This numerical flux differs from the one obtained in Ref. [21] as it takes into account the media discontinuity, which is required to solve the underlying vibroacoustic problems. The upwind numerical flux can be written as:

$$\boldsymbol{n}\cdot\boldsymbol{F}^* = \boldsymbol{n}\cdot\boldsymbol{F} + \boldsymbol{C}[\boldsymbol{q}_a] \tag{A.1}$$

$$\boldsymbol{C} = \frac{-1}{Z^+ + Z^-}\begin{bmatrix} \frac{Z^+Z^-n_x^2}{\rho_0^-} & \frac{Z^+Z^-n_xn_y}{\rho_0^-} & \frac{Z^+Z^-n_xn_z}{\rho_0^-} & \frac{-Z^-n_x}{\rho_0^-} \\ \frac{Z^+Z^-n_xn_y}{\rho_0^-} & \frac{Z^+Z^-n_y^2}{\rho_0^-} & \frac{Z^+Z^-n_yn_z}{\rho_0^-} & \frac{-Z^-n_y}{\rho_0^-} \\ \frac{Z^+Z^-n_xn_z}{\rho_0^-} & \frac{Z^+Z^-n_yn_z}{\rho_0^-} & \frac{Z^+Z^-n_z^2}{\rho_0^-} & \frac{-Z^-n_z}{\rho_0^-} \\ -K_0^-Z^+n_x & -K_0^-Z^+n_y & -K_0^-Z^+n_z & K_0^- \end{bmatrix}, \tag{A.2}$$

where $[\boldsymbol{q}_a] = \boldsymbol{q}_{ah}^+ - \boldsymbol{q}_{ah}^-$ is the jump between interior and exterior acoustic variables. The interior Bulk modulus is $K_0^- = \rho_0^-(c_0^-)^2$. The internal and external impedance are $Z^- = \rho_0^- c_0^-$ and $Z^+ = \rho_0^+ c_0^+$, respectively.

Appendix B. Impact sound radiation solution

The modal expansion method is widely used to solve the coupling problem between sound in a cuboid cavity and a panel vibration. There are two approaches that are commonly used. The first approach uses modal functions to expand the velocity potential that satisfies the velocity continuity and pressure over the panel surface [6,37]. The second technique uses the rigid-walled acoustic modes as the basis functions to expand the velocity potential [7–9].

The issue of the second approach is the velocity continuity over the panel that are not mathematically satisfied due to the use of the rigid-walled acoustic modes. However, the second approach is computationally more convenient. Hu et al. [38] have shown that both techniques were converged to the same solution as long as a sufficient number of modes were used in the second approach. In this appendix, the sound pressure under a slab is calculated based on Refs. [9,39] following the second technique as a comparison for the nodal DG solution. The slab vibration is modelled by the first shear deformation theory (FSDT).

B.1. Sound field

Consider the room (the air domain) in Fig. 2a as V enclosed by surface A, where $A = A_R \cap A_C$. The A_R and A_C are the surfaces with rigid walls and the concrete slab, respectively. The sound field in V satisfies the sound wave equation:

$$\nabla^2\phi = \frac{1}{c_0^2}\frac{\partial^2\phi}{\partial t^2}, \tag{B.1}$$

$$\frac{\partial\phi}{\partial n} = 0 \text{ on } A_R, \frac{\partial\phi}{\partial n} = \dot{w}^a \text{ on } A_C,$$

where ϕ is the velocity potential, c_0 is the sound speed, and $\dot{w}^a$ is the air particle velocity on A_C, and $(\cdot)$ denotes the derivative to time. The sound pressure inside V can be obtained as $p = -\rho_0\dot{\phi}$, with ρ_0 is the air density. Solutions of the Equation (B.1) with only rigid BCs are $\phi = \Phi_n \exp(i\hat{\omega}_n t)$ with $n \in [0, 1, ...]$. Φ_n are the room mode functions with index n that satisfy:

$$\nabla^2\Phi_n = -\left(\frac{\hat{\omega}_n}{c_0}\right)^2\Phi_n, \tag{B.2}$$

$$\frac{\partial\Phi_n}{\partial n} = 0,$$

$$\int_V \Phi_r\Phi_n \,\mathrm{dV} = \begin{cases} = 0, \text{for}, r \neq n, \\ = \Lambda_n^A, \text{for } r = n, \end{cases}$$

with $\hat{\omega}_n$ are the natural angular frequencies of the room with rigid BCs. Having the room mode functions Φ_n, Equation (B.1) can be transformed following the second Green's identity as in Ref. [9]:

$$\int_V \frac{\Phi_n}{c_0^2}\left(\ddot{\phi} + \hat{\omega}_n^2\phi\right)\mathrm{dV} = \int_{A_F}\Phi_n\dot{w}^a \mathrm{dS}. \tag{B.3}$$

To complete the interaction with the slab vibration on surface A_F, the air particle velocity ($\dot{w}^a$) should be equal to the velocity of the slab ($\dot{w}^s$) on surface A_C.

B.2. Structural vibration

In this subsection, the velocity of the slab ($\dot{w}^s$) on surface A_C is calculated. Following the first shear deformation theory (FSDT) [40], the slab displacement (w^s) in Fig. 2a follows:

$$I_0\ddot{w}^s + L(w^s, \varphi^x, \varphi^y) = U - \rho_0\dot{\phi}, \tag{B.4}$$

where L is a differential operator (see [41]), with φ^x and φ^y are the bending rotations with respect to the x- and y -directions, respectively. $I_0 = \rho_c h$ with ρ_c and h are the slab's density and thickness, and U is the excitation force.

The homogeneous solutions for Equation (B.4) can be written as $w^s = \psi_m \exp(i\omega_m t)$, for $m \in [1, 2, ...]$. The slab mode functions ψ_m satisfy:

$$L(\psi_m, \Psi_m^x, \Psi_m^y) = I_0\omega_m^2\psi_m, \tag{B.5}$$

where ω_m are the angular natural frequencies of the slab, with m as the index of each natural frequencies. The ψ_m, Ψ_m^x, and Ψ_m^y are the mode functions for the displacement, and the two bending rotations. They are orthogonal functions, and their exact expressions for the simply-supported BCs can be found in Ref. [41]. These functions are given in the next subsection to calculate the interaction with the acoustic modes.

B.3. Modal interaction

To have the coupling conditions, the displacement (w^s), force excitation (U), and the velocity potential (ϕ) can be expanded using the slab (ψ_p) and room mode functions (Φ_n) as:

$$w^s = \sum_{m=1}^{\infty} w_m^s(t)\psi_p(\boldsymbol{x}_{A_F}), \tag{B.6}$$

$$U = \sum_{m=1}^{\infty} U_m(t)\psi_p(\boldsymbol{x}_{A_F}), \tag{B.7}$$

$$\phi = \sum_{n=0}^{\infty} \phi_n(t)\Phi_n(\boldsymbol{x}). \tag{B.8}$$

Afterwards, Equations (B.6) and (B.7) are substituted to Equation (B.4). Equation (B.4) then multiplied with ψ_q and integrated over the A_F to obtain:

$$\ddot{w}_m^s + \omega_m^2 w_m^s = \frac{U_m}{I_0} - \frac{\rho_0}{I_0\Lambda_m^F}\sum_{n=0}^{\infty} L_{mn}\dot{\phi}_n, \tag{B.9}$$

$$\Lambda_m^F = \int_{A_F} \psi_m^2(\boldsymbol{x}_{A_F})\,\mathrm{dS}, \tag{B.10}$$

$$L_{mn} = \int_{A_F} \psi_m(\boldsymbol{x}_{A_F})\Phi_n(\boldsymbol{x})\,\mathrm{dS}.$$

Equations (B.6) and (B.8) are substituted to Equation (B.3) to obtain:

$$\ddot{\phi}_n + \omega_n^2\phi_n = \frac{c_0^2}{\Lambda_n^A}\sum_{m=1}^{\infty} L_{nm}\dot{w}_m^s, \tag{B.11}$$

$$\Lambda_n^A = \int_V \Phi_n^2(\boldsymbol{x})\,\mathrm{dV}, \tag{B.12}$$

$$L_{nm} = \int_{A_F} \Phi_n(\boldsymbol{x})\psi_m(\boldsymbol{x}_{A_F})\,\mathrm{dS}.$$

L_{nm} is the coupling coefficient between structure vibration and sound field mode functions. The mode functions are:

$$\psi_m(\boldsymbol{x}_{A_F}) = \sin\left(\frac{m_1\pi x}{L_x}\right)\sin\left(\frac{m_2\pi y}{L_y}\right),$$

$$\Phi_n(\boldsymbol{x}) = \cos\left(\frac{n_1\pi x}{L_x}\right)\cos\left(\frac{n_2\pi y}{L_y}\right)\cos\left(\frac{n_3\pi z}{L_z}\right)$$

with $m_1, m_2 \in [1, 2, ...]$ represent the anti-nodes of the mode functions in x and y -directions of the slab, respectively. L_x, L_y, L_z are the length, width, and height of the room. $n_1, n_2, n_3 \in [0, 1, ...]$ represents the number of nodes of mode functions in x, y and z-directions of the room, respectively. The integration in Equations (B.10) and (B.12) are:

$$\Lambda_m^F = \frac{L_x L_y}{4},$$

$$\Lambda_n^A = \begin{cases} L_x L_y L_z & \text{if } n_1 = n_2 = n_3 = 0, \\ \frac{L_x L_y L_z}{2} & \text{if } n_i = n_j = 0, \,\&\, n_k > 0, \\ \frac{L_x L_y L_z}{4} & \text{if } n_i = 0, \,\&\, n_j, n_k > 0, \\ \frac{L_x L_y L_z}{8} & \text{if } n_1, n_2, n_3 > 0, \end{cases}$$

and the coupling coefficient can be obtained as:

$$L_{mp} = \frac{L_x L_y}{4\pi^2}\left[\frac{1-(-1)^{(n_1-m_1)}}{(n_1-m_1)} - \frac{1-(-1)^{(n_1+m_1)}}{(n_1+m_1)}\right]\times \left[\frac{1-(-1)^{(n_2-m_2)}}{(n_2-m_2)} - \frac{1-(-1)^{(n_2+m_2)}}{(n_2+m_2)}\right].$$

Remark that in case of $(n_1 + m_1)$ or $(n_2 + m_2)$ is even, the $L_{nm} = 0$. It means that there is no interaction between the slab and the room. Afterwards, assuming a steady-state condition at angular frequency ω, Equations (B.9) and (B.11) can be written as:

$$I_0(\omega_m^2 - \omega^2)w_m^s + \frac{i\omega\rho_0}{\Lambda_m^F}\sum_{n=0}^{\infty} L_{mn}\phi_n = U_m \tag{B.13}$$

$$(\hat{\omega}_n^2 - \omega^2)\phi_n - \frac{i\omega c_0^2}{\Lambda_n^A}\sum_{m=1}^{\infty} L_{nm}w_m^s = 0 \tag{B.14}$$

These equations, can be written in matrix form as follows:

$$\left[\begin{array}{c|c} \boldsymbol{I^S} & \boldsymbol{C^A} \\ \hline \boldsymbol{C^S} & \boldsymbol{I^A} \end{array}\right]\left[\begin{array}{c} \boldsymbol{W^S} \\ \hline \boldsymbol{\Phi^A} \end{array}\right] = \left[\begin{array}{c} \boldsymbol{U^S} \\ \hline \boldsymbol{0} \end{array}\right],$$

$$\boldsymbol{W^S} = \begin{bmatrix} w_1^s \\ w_2^s \\ \vdots \\ w_m^s \end{bmatrix}; \boldsymbol{\Phi^A} = \begin{bmatrix} \phi_1 \\ \phi_2 \\ \vdots \\ \phi_n \end{bmatrix}; \boldsymbol{U^S} = \begin{bmatrix} U_1 \\ U_2 \\ \vdots \\ U_p \end{bmatrix},$$

$$\boldsymbol{C^A} = i\omega\rho_0\begin{bmatrix} \frac{L_{11}^T}{\Lambda_1^F} & \frac{L_{12}^T}{\Lambda_1^F} & \cdots & \frac{L_{1n}^T}{\Lambda_1^F} \\ \frac{L_{21}^T}{\Lambda_2^F} & \frac{L_{22}^T}{\Lambda_2^F} & \ddots & \vdots \\ \vdots & \ddots & \ddots & \vdots \\ \frac{L_{m1}^T}{\Lambda_m^F} & \frac{L_{m2}^T}{\Lambda_m^F} & \cdots & \frac{L_{mn}^T}{\Lambda_m^F} \end{bmatrix},$$

$$\boldsymbol{C^S} = -i\omega c_0^2\begin{bmatrix} \frac{L_{11}}{\Lambda_1^A} & \frac{L_{12}}{\Lambda_1^A} & \cdots & \frac{L_{1m}}{\Lambda_1^A} \\ \frac{L_{21}}{\Lambda_2^A} & \frac{L_{22}}{\Lambda_2^A} & \ddots & \vdots \\ \vdots & \ddots & \ddots & \vdots \\ \frac{L_{n1}}{\Lambda_n^A} & \frac{L_{n2}}{\Lambda_n^A} & \cdots & \frac{L_{nm}}{\Lambda_n^A} \end{bmatrix},$$

$$\boldsymbol{I^S} = I_0\begin{bmatrix} (\omega_1^2 - \omega^2) & 0 & \cdots & 0 \\ 0 & (\omega_2^2 - \omega^2) & \ddots & \vdots \\ \vdots & \ddots & \ddots & 0 \\ 0 & \cdots & 0 & (\omega_m^2 - \omega^2) \end{bmatrix},$$

$$\boldsymbol{I^A} = \begin{bmatrix} (\hat{\omega}_1^2 - \omega^2) & 0 & \cdots & 0 \\ 0 & (\hat{\omega}_2^2 - \omega^2) & \ddots & \vdots \\ \vdots & \ddots & \ddots & 0 \\ 0 & \cdots & 0 & (\hat{\omega}_n^2 - \omega^2) \end{bmatrix}.$$

Using this matrix-form, each modal coefficient in Equations (B.1)-(B.6) can be obtained using MATLAB to evaluate the sound pressure inside the room.

References

[1] Vorländer M, Schröder D, Pelzer S, Wefers F. Virtual reality for architectural acoustics. J Build Perform Simul 2015;8(1):15–25.
[2] Pind F, Jeong C-H, Sampedro Llopis H, Kosikowski K, Stromann-Andersen J. Acoustic virtual reality - methods and challenges. In: Baltic-nordic acoustics meeting (BNAM); 2018.
[3] Bilbao S, Hamilton B. Passive volumetric time domain simulation for room acoustics applications. J Acoust Soc Am 2019;145(4):2613–24.
[4] Thydal T, Pind F, Jeong C-H, Engsig-Karup AP. Experimental validation and uncertainty quantification in wave-based computational room acoustics. Appl Acoust 2021;178:107939.
[5] Toyoda M, Sakayoshi Y. Filter and correction for a hybrid sound field analysis of geometrical and wave-based acoustics. Acoust Sci Technol 2021;42(4):170–80.
[6] Bhattacharya MC, Crocker MJ. Forced vibration of a panel and radiation of sound into a room. Acta Acust Acust 1969;22(5).
[7] Fahy FJ. Vibration of containing structures by sound in the contained fluid. J Sound Vib 1969;10(3).
[8] Dowell EH, Gorman G, Smith D. Acoustoelasticity: general theory, acoustic natural modes and forced response to sinusoidal excitation, including comparisons with experiment. J Sound Vib 1977;52(4).
[9] Bokil V, Shirahatti US. A technique for the modal analysis of sound-structure interaction problems. J Sound Vib 1994;173(1).
[10] Rindel JH. Sound insulation in buildings. CRC Press; 2018.
[11] Cambridge JE. An evaluation of various sound insulation software and their applications in the design of silent rooms. Master's thesis. Chalmers University of Technology; 2006.
[12] Maluski SPS, Gibbs BM. Application of a finite-element model to low-frequency sound insulation in dwellings. J Acoust Soc Am 2000;108(4).
[13] Brunskog J, Davidsson P. Sound transmission of structures. a finite element approach with simplified room description. Acta Acust Acust 2004;90(5).
[14] Davidsson P, Brunskog J, Wernberg P-A, Sandberg G, Hammer P. Analysis of sound transmission loss of double-leaf walls in the low-frequency range using the finite element method. Build Acoust 2004;11(4).
[15] Arjunan A, Wang C, Yahiaoui K, Mynors D, Morgan T, Nguyen V, et al. Development of a 3d finite element acoustic model to predict the sound reduction index of stud based double-leaf walls. J Sound Vib 2014;333(23).
[16] Yang Y, Kingan MJ, Mace BR. A wave and finite element method for calculating sound transmission through rectangular panels. Mech Syst Signal Process 2021;151:107357.
[17] Toyoda M, Takahashi D. Prediction for architectural structure-borne sound by the finite-difference time-domain method. Acoust Sci Technol 2009;30(4).
[18] Ferreira N. Vibroacoustics modelling using the finite difference time domain method: incorporating porous materials and mechanically excited plates. Ph.D. thesis. University of Liverpool; 2019.
[19] Modave A, St-Cyr A, Warburton T. Gpu performance analysis of a nodal discontinuous Galerkin method for acoustic and elastic models. Comput Geosci 2016;91:64–76.
[20] Wang H, Cosnefroy M, Hornikx M. An arbitrary high-order discontinuous Galerkin method with local time-stepping for linear acoustic wave propagation. J Acoust Soc Am 2021;149(1).
[21] Wang H, Sihar I, Pagán Muñoz R, Hornikx M. Room acoustics modelling in the time-domain with the nodal discontinuous Galerkin method. J Acoust Soc Am 2019;145(4).
[22] Wang H, Yang J, Hornikx M. Frequency-dependent transmission boundary condition in the acoustic time-domain nodal discontinuous Galerkin model. Appl Acoust 2020;164:107280. https://doi.org/10.1016/j.apacoust.2020.107280.
[23] Pind F, Jeong C-H, Engsig-Karup A, Hesthaven J, Strømann-Andersen J. Time-domain room acoustic simulations with extended-reacting porous absorbers using the discontinuous Galerkin method. J Acoust Soc Am 2020;148(5).
[24] Wang H, Hornikx M. Extended reacting boundary modeling of porous materials with thin coverings for time-domain room acoustic simulations. J Sound Vib 2023;548:117550.
[25] Sihar I, Hornikx M. Implementation of the nodal discontinuous Galerkin method for the plate vibration problem using linear elasticity equations. Acta Acust Acust 2019;105(4).
[26] Sihar I, Yang J, Hornikx MC. Discontinuous Galerkin method for vibration of structures with piecewise constant material properties. Appl Acoust Jan. 2024;216. https://doi.org/10.1016/j.apacoust.2023.109793.
[27] Käser M, Dumbser M. A highly accurate discontinuous Galerkin method for complex interfaces between solids and moving fluids. Geophysics 2008;73(3).
[28] Shukla K, Carcione JM, Hesthaven JS, L'heureux E. Waves at a fluid-solid interface: explicit versus implicit formulation of boundary conditions using a discontinuous Galerkin method. J Acoust Soc Am 2020;147(5).
[29] Wilcox LC, Stadler G, Burstedde C, Ghattas O. A high-order discontinuous Galerkin method for wave propagation through coupled elastic-acoustic media. J Comput Phys 2010;229(24):9373–96.
[30] Zhan Q, Ren Q, Zhuang M, Sun Q, Liu QH. An exact Riemann solver for wave propagation in arbitrary anisotropic elastic media with fluid coupling. Comput Methods Appl Mech Eng 2018;329.
[31] Pierce AD. Acoustics-an introduction to its physical principles and applications. Cham: Springer; 2019.
[32] LeVeque RJ. Finite volume methods for hyperbolic problems. Cambridge: Cambridge Unversity Press; 2004.
[33] Hesthaven J. Nodal discontinuous Galerkin methods: algorithms, analysis, and applications. New York: Springer; 2008.
[34] Toulorge T. Efficient Runge-Kutta discontinuous Galerkin methods applied to aeroacoustics. Ph.D. thesis. Katholieke Universiteit Leuven; 2012.
[35] Bermúdez A, Hervella-Nieto L, Rodríguez R. Finite element computation of three-dimensional elastoacoustic vibrations. J Sound Vib 1999;219(2).
[36] COMSOL AB, COMSOL Multiphysics ® version 5.4, 2018.
[37] Pretlove AJ. Free vibrations of a rectangular panel backed by a closed rectangular cavity. J Sound Vib 1965;2(3).
[38] Hu Z, Maxit L, Cheng L. Convergence criteria on the acoustic velocity continuity in a panel-cavity system. J Acoust Soc Am 2017;141(3).
[39] Fahy F, Gardonio P. Sound and structural vibration: radiation, transmission and response. 2nd edition. Academic Press; 2007.
[40] Reddy JN. Theory and analysis of elastic plates and shells. 2nd edition. Florida: CRC Press; 2007.
[41] Wang CY, Wang CM. Structural vibration: exact solutions for strings, membranes, beams, and plates. Taylor & Francis; 2013.